# ANALYSIS OF MULTIANGLE IMAGING SPECTRORADIOMETER (MISR) MEASUREMENTS IN THE QUEENSLAND SOUTHERN BRIGALOW BELT

**John D. Armston[†*], Stuart R. Phinn*, Peter F. Scarth[†] and Tim J. Danaher[†]**

[†] Natural Resource Sciences
Queensland Department of Natural Resources and Mines
80 Meiers Road, Indooroopilly, Queensland, Australia, 4068
Phone +61 7 3896 9696 Fax +61 7 3896 9843
john.armston@nrm.qld.gov.au

* Centre for Geographic Information Science and Applications
School of Geography, Planning and Architecture
University of Queensland, Brisbane, Queensland, Australia, 4072.

## Abstract

Many theoretical and applied studies have demonstrated that the anisotropic reflectance of the land surface can be used to characterise the structural and optical properties of vegetation. The Multi-angle Imaging SpectroRadiometer (MISR) has the potential to characterise vegetation structure and consequently improve the operational monitoring of vegetation structure in Queensland. The aim of this pilot investigation was to produce a quantitative comparison of MISR multiple view angle (MVA) measurements and vegetation structure for the Southern Brigalow Belt (SBB) Biogeographic Region. Airborne LIDAR data was used to estimate foliage projective cover (FPC) at the spatial resolution of MISR and was validated using coincident field data. Coefficients describing the shape of the bidirectional reflectance distribution function (BRDF) were derived by inversion of the linear Ross-Thick Li-Sparse Reciprocal and the non-linear Rahman-Pinty-Verstraete (RPV) models against a time series of MISR "Local Mode" surface bidirectional reflectance factor (BRF) data. Comparison of model inversion accuracy and correlation with FPC revealed the RPV model coefficients were related to spatial and temporal variations in vegetation structure in the Queensland SBB and are consistent with published findings. The application of these data to the operational monitoring of woody and herbaceous vegetation cover and change in Queensland is currently undergoing further quantitative evaluation.

## Introduction

Vegetation structure is defined here as "the horizontal and vertical distribution of components within a plant community" (Jupp and Walker, 1996). The structure of vegetation is indicative of the climatic, ecological and disturbance

events or regimes that shape a plant community, hence it is recognised as an important component in vegetation dynamics (Specht and Specht, 1999). Recognition of this importance at regional and continental scales, especially in terms of climate and land management, has resulted in the use of satellite remote sensing for operational mapping of vegetation structure in Australia (Henry *et al.*, 2002). The Statewide Landcover and Trees Study (SLATS) have pioneered the application of remote sensing to this problem in Queensland, Australia (Danaher *et al.*, 1998).

Land surface apparent reflectance is dependent on wavelength, illumination and sensor view geometry, and is determined by the structural and optical characteristics of the land surface. This dependence is described by the bidirectional reflectance distribution function (BRDF) (Martonchik *et al*., 2000). In operational remote sensing applications, the BRDF is often viewed as a source of error that needs correction before quantitative data on vegetation structure such as foliage projective cover (FPC) are derived (e.g. Danaher, 2002). SLATS currently only uses spectral reflectance variations for detecting vegetation structure (Danaher *et al*., 2004), however the anisotropic reflectance of vegetation canopies potentially offers more information directly related to vegetation structure (Asner *et al*., 1998).

In order to capture BRDF related information, multiple view angle (MVA) observations are needed. The Multi-angle Imaging SpectroRadiometer (MISR) instrument aboard the EOS-Terra platform is unique as it can acquire quasi-simultaneous 275 m spatial resolution observations of the land surface at 672 nm (visible red) with view angles of 0° (Nadir), 26.1° (A), 45.6° (B), 60° (C), and 70.5° (D) in the forward (f) and aftward (a) directions, and also at 446, 558, and 866 nm for nadir only (Figure 1). The remaining view angles for these spectral bands are typically at 1100 m spatial resolution. This data acquisition strategy is referred to as “Global” mode. MISR can acquire 275 m spatial resolution data in all spectral bands in “Local” mode, however for an approximately 300 km path only due to the volume of data generated (Diner *et al.*, 1998).

Lovell and Graetz (2002) and Grant (2000) were able to discriminate between vegetation structural formations over the Australian continent in a comparison of coarse spatial resolution (6 km $\times$ 7 km) POLDER I data and the independently mapped AUSLIG structural formation classification (AUSLIG, 1990). This study required independent and coincident data describing attributes of vegetation structure at a finer scale, for which Airborne LIght Detection And Ranging (LIDAR) was directly applicable. LIDAR is an active remote sensing system that operates by emitting light pulses and measuring the time it takes to reflect off vegetation foliage layers and the ground surface and return to the sensor. Based on the time distribution and range of returns, a representation of vegetation structure is obtained (e.g. Lovell *et al.*, 2003). LIDAR systems typically operate in the near-infrared (900 to 1064 nm), with current Australian commercial airborne sensors recording only discrete portions (typically first and last) above a detection threshold of each return using a small footprint (*e.g.* 25 cm). LIDAR is used in this study as a sampling tool, not a mapping tool, to characterise vegetation structure at the MISR pixel scale.

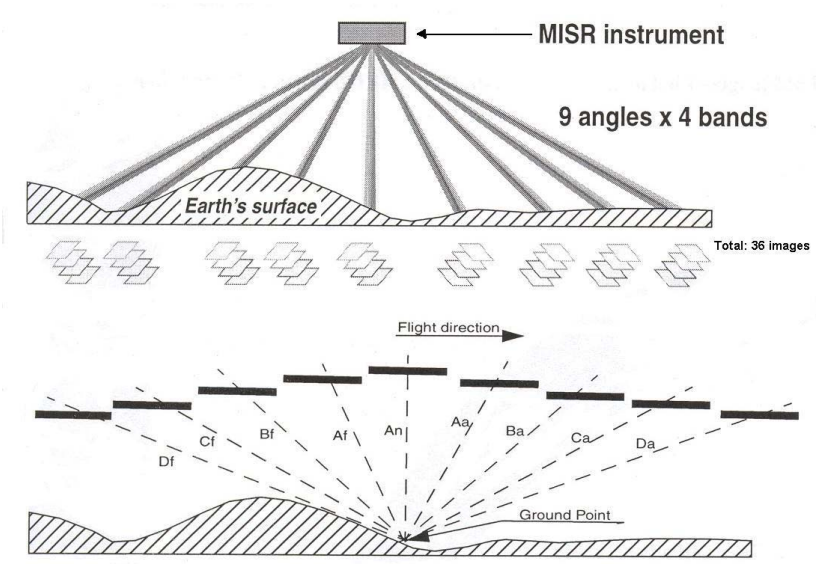


**Figure 1** The MISR is on board the EOS-Terra satellite and views the land surface at nine angles: 0° (An), 26.1° (A), 45.6° (B), 60° (C), and 70.5° (D) in the forward (f) and aftward (a) directions. All nine cameras view a single location within approximately seven minutes (from Diner *et al.*, 1999).

The aim of this study is to assess the empirical relationship between the BRDF and the structure of vegetation in the SBB biogeographic region. This information will provide a preliminary assessment of the potential of MISR MVA measurements for improving the operational monitoring of vegetation by SLATS in Queensland. The three primary objectives are outlined below.

1. Estimate MISR local mode pixel scale FPC using field and LIDAR data;
2. Determine the BRDF typology of the land surface in the Queensland SBB Biogeographic Region using a time series of MISR acquisitions;
3. Compare measures of the spectral directional reflectance of the land surface to LIDAR derived estimates of FPC.

## Study Site

The Brigalow Belt (BB) bioregion covers 367,404 km$^2$ and the landscape is a mosaic of cleared fields, woodland and forest communities which includes areas that are remnant, in degradation and/or regeneration. Vegetation communities include *Acacia harpophylla* (brigalow) forest and woodland, eucalypt forest and woodland, grassland, dry rainforest, *Callitris glaucophylla* (cypress pine) woodland, and riparian communities. The study site (Figure 2) was selected because previous studies have indicated that the area is representative of the variation in vegetation structure and disturbances in the SBB biogeographic region (Lucas *et al.*, 2001). Secondly, LIDAR and field data including FPC that were acquired in late July / early August 2000 over the study site were made available for this study.

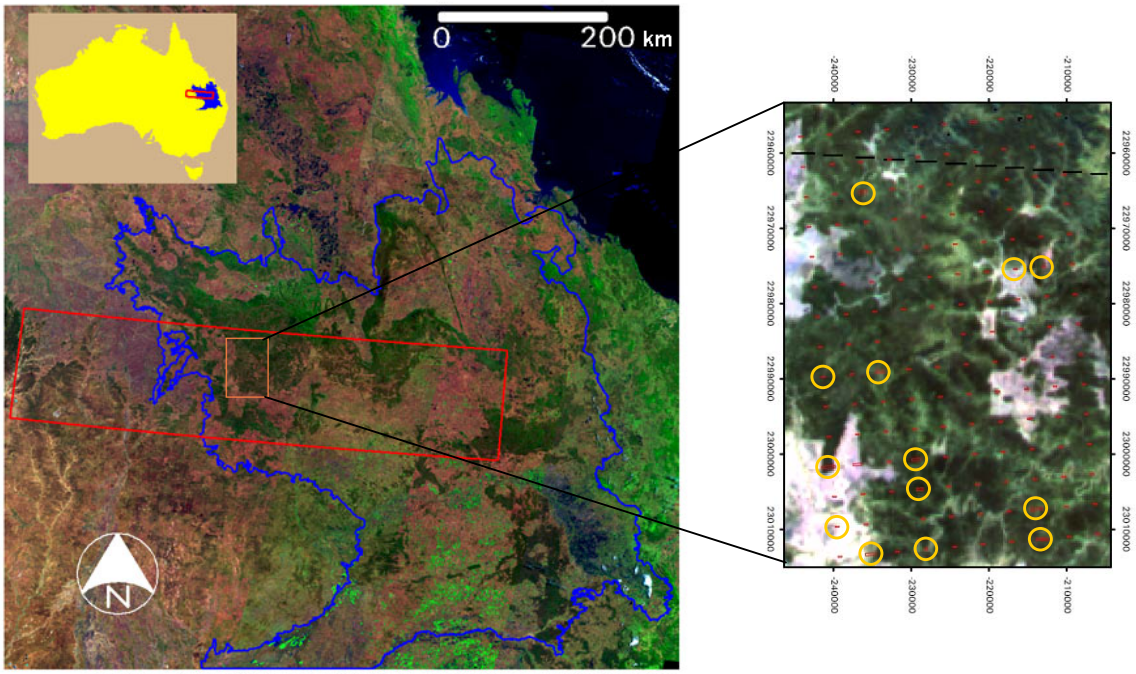



**Figure 2** The SBB Biogeographical Region is shown by the blue polygon. A MISR scene (Block 111) is shown by the red polygon. The study site is the region within the orange polygon. The background is a mosaic of Landsat-7 ETM+ scenes (RGB Bands 5-4-2). Inset: The location of LIDAR plots in the study site (field subplots are circled) over local mode MISR data (RGB 60º F - Nadir - 60º B false colour composite).

## Methodology

*MISR Data Acquisition and Preprocessing*

MISR Level 1B2 Terrain Projected Radiance, Level 1B Geometric Parameters, and Level 2 Land Surface Products covering the study area were acquired through the Earth Observing System (EOS) Data Gateway at the National Aeronautics and Space Administration (NASA) Langley Atmospheric Sciences Data Centre. The Level 1B2 Terrain Projected Radiance data was acquired in Local Mode. Acquisitions contaminated by cloud or that were predominantly missing data in the Level 2 product were excluded. The time series of MISR Local Mode data analysed for this study this study is listed in Table 1.

**Table 1** Terra orbit, date WRS-2 path, processing version and estimated cloud cover for Local Mode MISR data acquired for MISR Block 111.

| Terra Orbit | Date | WRS-2 Path | Processing Version |
|---|---|---|---|
| 18125 | 15/05/2003 | 92 | 20 |
| 18227 | 22/05/2003 | 93 | 20 |
| 18460 | 07/06/2003 | 93 | 20 |
| 19028 | 16/07/2003 | 94 | 20 |
| 19159 | 25/07/2003 | 93 | 20 |
| 19261 | 01/08/2003 | 94 | 20 |
| 20091 | 27/09/2003 | 93 | 20 |

The MISR data were preprocessed to produce Space Oblique Mercator rasters of 275m spatial resolution "at-sensor" physical radiance $L$($W\ m^{-2}\ sr^{-1}\ \mu m^{-1}$) in and 1100m spatial resolution surface bi-directional reflectance factor (BRF) ($\theta_r, \phi_r, \theta_i, \phi_i, \lambda$) in the blue, green, red and NIR spectral bands. 275m spatial resolution TOA BRF was calculated from "at-sensor" physical radiance using Equation 1 (Martonchik *et al.*, 2000).

$$\rho_\lambda = \frac{\pi \cdot d^2 \cdot L_\lambda}{E_{O\lambda} \cdot \cos\theta_i} \qquad \text{Equation 1}$$

For band $\lambda$, $\rho$ is TOA BRF, $d$ is solar distance in $AU$, $E_O$ is exo-atmospheric solar irradiance, and $\theta_i$ is the solar zenith angle. The next step was to derive surface BRF at 275m spatial resolution by removing the atmospheric component of this "apparent" reflectance. Due to the limited scope of this study, it was important to use existing atmospherically corrected data where possible so an approach was devised to calibrate the Local Mode TOA BRF to the MISR Level 2 surface BRF product. In order to preserve the spatial variation in the relationship between TOA BRF and surface BRF and smooth the spatial irregularities in the MISR Level 2 surface BRF product, Ordinary Least-Squares (OLS) regression was applied in a moving window approach (Figure 3).

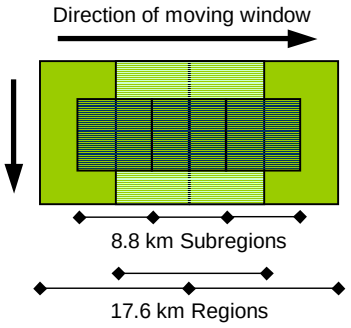


1. Each region is 17.6 km by 17.6 km
   - TOA BRF 275 m by 275 m pixels
   - Surface BRF 1100 m by 1100 m pixels
2. TOA BRF block averaged to 1100 m by 1100 m pixels
3. OLS regression between the two regions
4. Regression equation inverted against 8.8 km by 8.8 km TOA BRF pixels subregion.
5. Regression window moves along image 8.8km.
6. This process is repeated for all regions in the X dimension then moves 8.8km down the Y dimension and proceeds across the X dimension again.

**Figure 3** Method of moving-window OLS regression.

*Semi-empirical Models*

The semi-empirical models used in this study are the Rahman-Pinty-Verstraete (RPV) model (Rahman *et al.*, 1993), and the Ross-Thick Li-Sparse Reciprocal model (hereafter referred to as Ross-Li) from Version 3.3 of the Algorithm for Model Bidirectional Reflectance Anisotropies of the Land Surface (AMBRALS) (Lucht *et al.*, 2000). These models were selected to parameterise the BRDF due to the strong theoretical and empirical evidence showing they can be linked to vegetation structure (Gao *et al.*, 2003; Pinty *et al.*, 2002).

The four-parameter RPV model is a non-linear model consisting of a modified Minneart function, a Henyey-Greenstein phase function, and a function accounting for the hotspot (Equation 2) (Gobron and Lajas, 2002).

$$BRF_{RPV} = \rho_0 . \breve{\rho}(\theta_v, \theta_i, \phi; \rho_c, \Theta, k)$$ Equation 2

$\rho_0$ and $\breve{\rho}$ represent the spectral amplitude and anisotropy of the BRF, respectively. The RPV model represents the main aspects of the BRDF shape by separating it into overall brightness ($\rho_0$), bowl-bell shaped anisotropy ($k$), degree of forward or backward scattering ($\Theta$), and hotspot ($\rho_c$) components. $\rho_c$ controls the width of the hotspot and is usually assumed to equal $\rho_0$, reducing it to a three parameter model (Rahman *et al.,* 1993). Figure 4 illustrates these components along the principal plane (plane normal to the sun-sensor-target).

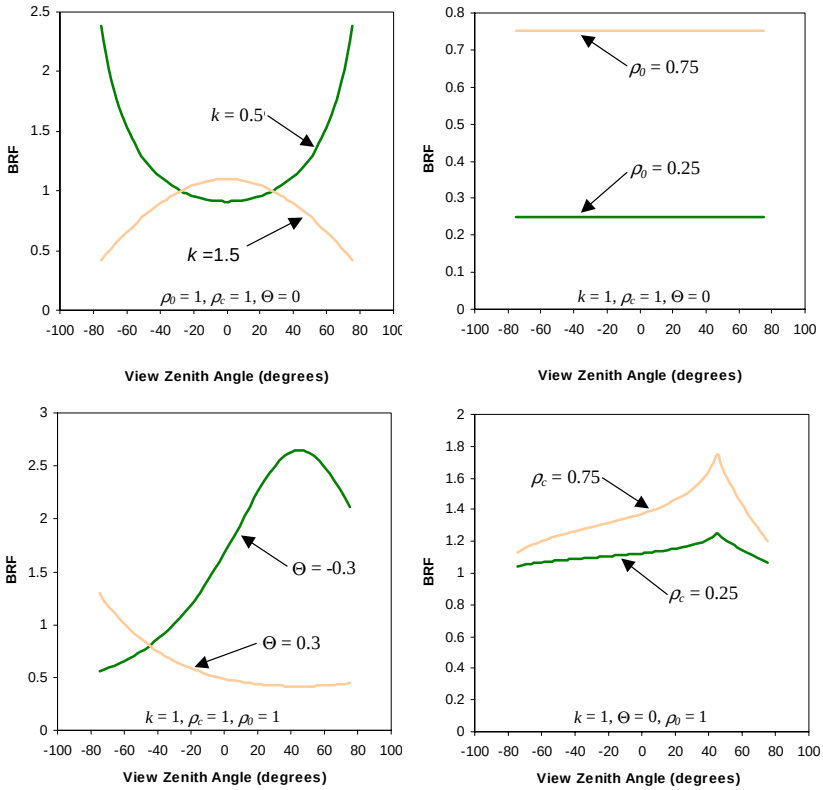


**Figure 4** RPV BRF model shape along principal plane with changing values of the $\rho_0$, $\rho_c$, $\Theta$ and $k$ coefficients (solar zenith 45°).

Linear kernel-driven models are a simplified physical representation of radiative scattering by land surfaces (Wanner *et al.*, 1995; Roujean *et al.*, 1992). They are an additive combination of kernels describing the independent contribution of isotropic, specular, volumetric and/or geometric scattering in a scene for any particular wavelength (Equation 3).

$$BRF_{Ross-Li} = f_{iso} + \left(f_{vol} \times k_{vol}(\theta_v, \theta_i, \phi)\right) + \left(f_{geo} \times k_{geo}(\theta_v, \theta_i, \phi)\right)$$ Equation 3

The terms $f_{iso}$, $f_{geo}$, and $f_{vol}$ are the spectrally dependent model parameters. The isotropic kernel is a constant, and the volumetric and geometric-optical kernels

are represented by the $k_{geo}$ and $k_{vol}$ terms, respectively. The Ross kernel is a single scattering approximation of a horizontally continuous low LAI (Ross-Thin) or high LAI (Ross-Thick) canopy, and assumes equal leaf transmittance and reflectance, uniform leaf angle distribution and a Lambertian background. The Li-Sparse Reciprocal kernel is an expression of the proportion of sunlit crown and background resulting from ellipsoids randomly distributed at height *h,* of horizontal radius *r*, and vertical radius *b* where mutual shadowing does not occur. The overlap between the areas of viewing and illumination shadow is dependent on the relative height *h/b*, and the relative shape *b/r* of crowns. This dependence results in different kernels for different *b/r* and *h/b*. In practice these are reduced to four cases for oblate (O) or prolate (P) crowns that are high (H) or low (L) (Wanner *et al.,* 1995). *b/r* and *h/b* were set to 2 and 1 (referred to as the MODIS case), respectively, according to Lucht *et al.* (2000). Figure 5 illustrates the kernel shapes along the principal plane.

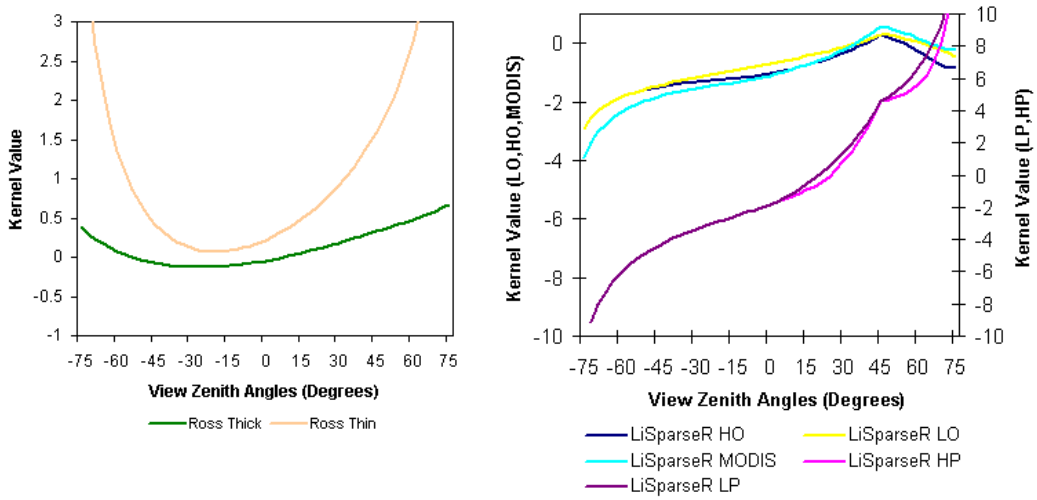


**Figure 5** Ross Thin, Ross Thick and Li-Sparse kernels along the principal plane (solar zenith 45°). Li-Sparse kernels are shown with different *b/r* and *h/b*. MODIS=MODIS operational *b/r* and *h/b*, H=High, P=Prolate, L=Low, and O=Oblate.

The Levenberg-Marquardt method as programmed in IDL® (RSI, 2004) as MPFIT by Markwardt (2002), was used for inversion of the RPV BRF model. AMBRALS uses LU decomposition as the matrix inversion method used for the linear inversion of the Ross-Li model (Lucht *et al.*, 2000). The error term minimised by AMBRALS is the Root Mean Square Error (RMSE) (Equation 4).

$$RMSE_{\lambda} = \sqrt{\frac{\sum_{i=1}^{N}\left(\rho_{i(measured)} - \rho_{i(modelled)}\right)^2}{N}} \qquad \text{Equation 4}$$

Where for band $\lambda$, $\rho_{i(measured)}$ is an individual surface BRF measurement for viewing direction *i*. $\rho_{i(modelled)}$ is the corresponding modelled surface BRF and *N* is the total number of surface BRF measurements (*i.e.* 9) for a given pixel.

In order to quantitatively test the validity and accuracy of the RPV and Ross-Thick Li-Sparse inversion results, a comparison of the modelled and observed BRF was conducted by using RMSE (Equation 4) as an indicator of inversion accuracy. This is the measure indicator of inversion accuracy that has been used in previous studies to verify the models used in this study (Maignan *et al.*, 2004; Hu *et al.*, 1997). The RMSE is divided by the mean of the BRF so it is expressed as a percentage. It is important to note that this accuracy analysis assumes measurement errors in the surface BRF are negligible.

It was probable that the land surface had not changed significantly during the temporal window of MISR acquisitions. However, the time series still provided an opportunity to assess whether there were any interpretable patterns, or lack thereof, in the time series of the BRF model coefficients. The NIR and red bands were used for this analysis, as these wavelengths represent the dominant scattering processes controlled by vegetation structure (Pinty *et al.*, 2002; Gao *et al.*, 2003). Similar to Lovell and Graetz (2002), plotting the time series and assessing the mean and standard deviation were deemed adequate tools for assessing the temporal variation in the BRF model coefficients.

*LIDAR Data Acquisition*

First and last return LIDAR data were acquired over a one-week period in August, 2000. Tickle *et al.* (2001) describes the LIDAR data in detail so only a brief summary is provided here. The acquisition specifications for the LIDAR data are listed in Table 2. Figure 2 shows the location of the LIDAR plots within the study site.

**Table 2** LIDAR data acquisition specifications.

| **LIDAR Acquisition** | **Specification** |
|---|---|
| System | Optech 1020 5 Hz NIR airborne laser scanner |
| Sample spacing | < 1.0 m |
| Beam divergence | 0.3 milliradians |
| Swath | > 200 m |
| Independent returns per second | 5000 |
| Aircraft | Bell Jet Ranger helicopter |
| Nominal altitude | 250 m |

For each LIDAR plot shown in Figure 2, there was a 500 m $\times$ 150 m area of LIDAR returns made available. The full areal extent of the LIDAR returns (~1000 m $\times$ ~200 m) was made available only for the LIDAR samples with field plots. Due to time constraints and the fact that no data on the scan angle of the LIDAR returns were directly available, it was assumed that all LIDAR returns were measured from the local normal.

*Field Measurements*

Lucas *et al.* (2001) describes the field data and sampling design so only a brief summary of the data used is provided here. Field measurements were

collected in late July and early August from 12 of the 150 150 m $\times$ 500 m plots over which LIDAR was acquired (Figure 2). Within these plots, 36 (50 m $\times$ 50 m) subplots were selected based on a random sampling scheme stratified using large-scale aerial photography. Within each subplot, FPC field measurements were recorded at 1m intervals along three parallel 50m transects using the tube and crosshair method described by Specht (1970). For each 1m interval, either green leaf, dead leaf, branch, or sky was recorded for the overstorey, and either green leaf, dead leaf, bare ground, litter or shrub was recorded for the understorey. FPC was calculated as the proportion of all point observations that were overstorey green leaf or shrub observations.

*Foliage Projective Cover*

The LIDAR returns were separated into ground and non-ground returns using a modified version of the progressive morphological filter of Zhang *et al.* (2003). Once the LIDAR returns were classified, the next step was to generate a canopy height model (CHM) where the height of each return above the ground surface is defined. This was achieved by generating a DTM from the ground returns using inverse distance weighted (IDW) interpolation. The height of each return above the ground surface is simply the elevation of each return minus the elevation of the ground at that coordinate.

The field FPC data was used to calibrate the LIDAR cover estimates (Equation 5) to FPC. Due to the lack of independent data, the LIDAR FPC estimates were validated using cross-validation. Excluding a random 10% of the data, calculating the calibration coefficients from the remaining 90%, and then applying the resulting equation to calibrate the excluded 10% of the data was the method of computation. This process was iterated until FPC for every field site was estimated independently.

$$\%COVER_{LIDAR} = \frac{100 \cdot N_C}{N_G + N_C} \qquad \text{Equation 5}$$

$N_C$ is the number of canopy returns and $N_G$ is the number of ground returns within a defined area. FPC was calculated for each LIDAR plot over an area representing 275 m east to west, and 150 m to 200 m north to south. This was the full spatial extent of LIDAR data available at MISR local mode resolution.

## Results and Discussion

*MISR*

Figure 6 presents a map showing MISR local mode surface BRF. Missing data within the study site is obvious, and is a result of missing data in the Global Mode surface BRF product that prevents the calibration of the Local Mode TOA BRF. Whilst the moving window OLS regression technique was effective in calibrating the Local Mode TOA BRF to the Global Mode surface BRF, it is important to note that it merely smeared the error existing in the MISR Level 2 surface BRF product. This study has made no attempt to correct for

atmospheric effects by modelling the interaction of light with the atmosphere. Atmospheric correction here was purely a calibration of one variable to another, therefore any limitations of the MISR Global Mode surface BRF product were inherited (see Abdou *et al.* 2002).

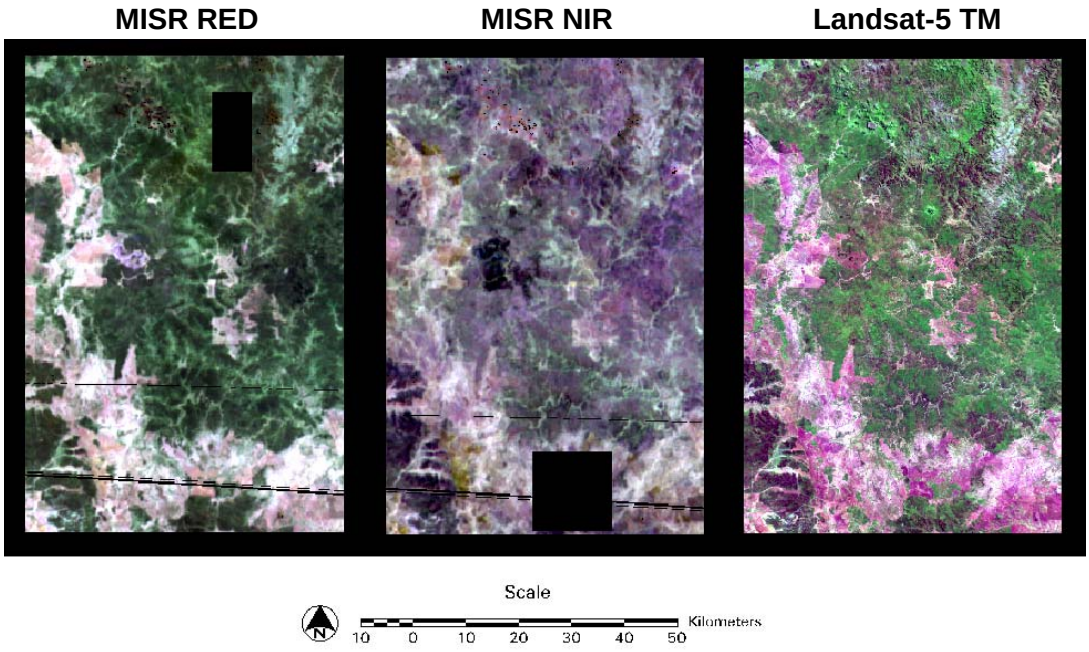


**Figure 6** Example Red and NIR surface BRF images for the 27/09/2003 acquisition over the study site. The images are multi-angular red (60º forward), green (nadir) and blue (60º backward) composites. A Landsat-5 TM image (18/08/2003) of the study site (Bands 5-4-2 RGB false colour composite) is also shown for comparison.

Table 3 shows a comparison of mean relative RMSE mean and standard deviation for three MISR local mode acquisitions acquired over different paths and under different solar zenith angles over the study site. Both models fit better at lower solar zenith angles and it is most pronounced for the Ross-Li model. The RPV model has a better fit than the Ross-Li model for all solar zenith angles and spectral bands. All mean relative RMSE's greater than 0.10 (10%), apart from blue band (15/05/2003 acquisition), resulted from the Ross-Li model. Finally, the NIR has a lower mean relative RMSE than all the other bands for both models.

The relative RMSE for the 15/05/2003 acquisition was large compared to the other acquisitions at lower solar zenith angles. The atmospheric correction results did not show anything inconsistent with the other acquisitions, however the azimuthal sampling for this acquisition is very close to the hotspot, which is where the sensor, sun and ground target are co-linear. This is unique among all the MISR acquisitions analysed in this study, and may indicate an inadequacy of the Ross-Li model in modelling the hotspot. This is consistent with Maignen *et al.* (2004), who found that the Ross-Li model was inadequate for modelling the hotspot as observed by the POLDER I instrument.

The poorer performance of the Ross-Li model at large solar zenith angles is possibly due to mutual shadowing, meaning shadows cast from crowns fall on adjacent crowns rather than on the background (Li and Strahler, 1992). In such cases, only the sunlit crown tops are visible from the larger zeniths view of MISR, which translates into a brightening of the BRF at larger view or solar zenith angles. The Li-Sparse kernel does not account for mutual shadowing, therefore its assumptions break down under these conditions (Wanner *et al.*, 1995). The Li-Dense kernel accounts for mutual shadowing, therefore it may provide a better fit to the MISR Local Mode acquisitions at large zenith angles (Wanner *et al.*, 1995).

**Table 3** Summary mean ($\bar{x}$) and standard deviation ($\sigma$) relative RMSE statistics describing the accuracy of the BRF model inversions. Errors greater than 10% of the mean BRF are highlighted red. "*" indicates missing data.

| Acquisition | Band | RPV | | Ross-Li | |
|---|---|---|---|---|---|
| | | $\bar{x}$ | $\sigma$ | $\bar{x}$ | $\sigma$ |
| 15/05/2003 | Blue | 0.129 | 0.034 | 0.301 | 0.045 |
| Path 92 | Green | 0.064 | 0.017 | 0.253 | 0.035 |
| SZA ~ 52° | Red | 0.053 | 0.015 | 0.248 | 0.039 |
| | NIR | 0.037 | 0.007 | 0.173 | 0.015 |
| 02/09/2003 | Blue | 0.062 | 0.019 | 0.088 | 0.023 |
| Path 94 | Green | 0.022 | 0.008 | 0.057 | 0.014 |
| SZA ~ 41° | Red | 0.039 | 0.013 | 0.061 | 0.016 |
| | NIR | 0.016 | 0.005 | 0.063 | 0.008 |
| 27/09/2003 | Blue | * | * | * | * |
| Path 93 | Green | 0.026 | 0.009 | 0.053 | 0.014 |
| SZA ~ 33° | Red | 0.030 | 0.011 | 0.056 | 0.018 |
| | NIR | 0.015 | 0.007 | 0.034 | 0.009 |

Figure 7 again shows that the RPV model fits better than the Ross-Li model. Of interest is the bimodal distribution shown in the red band, which suggests that areas of low foliage cover had a lower relative RMSE than areas of high foliage cover. In fact, the relative RMSE for low cover areas falls close to the 1:1 line with the RPV model. This is consistent with Hu *et al.* (1997) who found that the inversion accuracy of the Ross-Li model was dependent on land cover types for which they were designed, however acceptable fits were still found for most cover types. This is consistent with the results presented in Figure 7, as it is apparent that only outliers exceed 0.1 (10%) relative RMSE. Due to the better fit of the RPV and the violated assumptions of the Ross-Li models, only the results for the RPV coefficients are subsequently shown.

Figure 8 shows the spatial-temporal variation in the mean and standard deviation for the time series of the RPV BRF model coefficients. The $\Theta$ coefficient shows spatially consistent variations in the red band. The areas of higher foliage cover show up as red (≈-0.2) indicating strong backscattering simply due to shadow casting. The areas of lower foliage cover show up as yellow (≈-0.1) indicating relatively weaker backscattering. The green areas, however, appear to correspond to areas of relatively complex terrain so

interpretation based of vegetation structure is confounded. The standard deviation of the time series of the Θ coefficient appears to be dependent on land cover type, with wooded areas showing higher values. This is interpreted as varying proportions of sunlit background in response to changing solar zenith angle (Gerard and North, 1997).

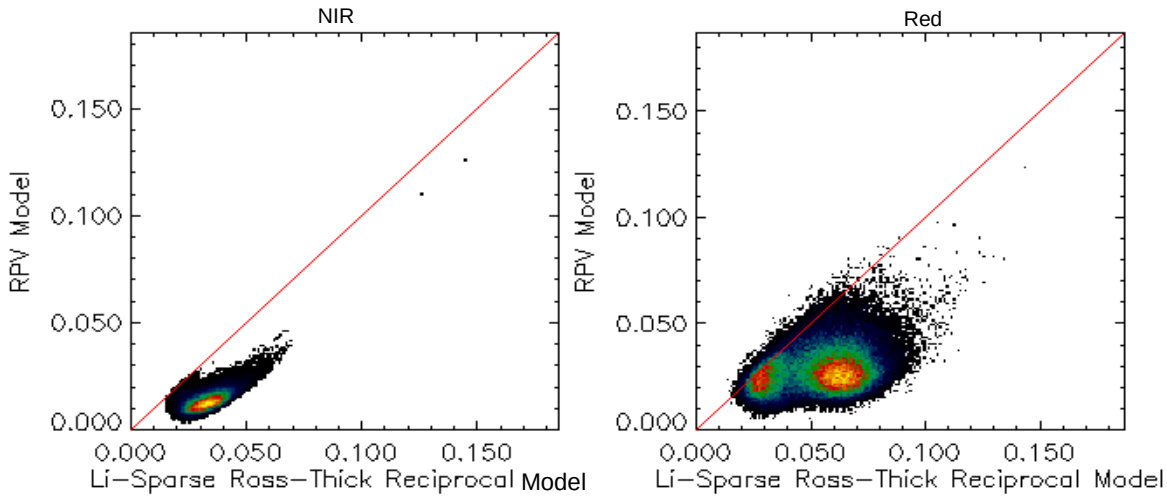


**Figure 7** Comparison of the relative RMSE for the Ross-Thick Li-Sparse Reciprocal and RPV BRF models for MISR acquisition 27/09/2003. 2D histograms are shown for the NIR and red spectral bands. The 1:1 line is shown in red.

The Θ coefficient in the NIR band shows relatively little spatial contrast in comparison to the red band, with much lower values (<-0.184). This indicates that surface anisotropy has been reduced due to high NIR reflectance of both vegetation and soils, and multiple scattering. The standard deviation reflects this with very little variation in the predominance of backscattering in wooded areas. Local peaks in standard deviation appear to correspond to water run-on areas (Australian 1:250,000 Topographic Map Sheet SG: 55-7) therefore these areas are probably subject to varying soil moisture and ground cover. Note that these areas are also observed in the isotropic coefficient, indicating that surface changes are being identified in both the spectral and angular domains.

The mean *k* coefficient, which describes the “bowl” or “bell” shaped anisotropy, shows consistent spatial variation in the red band, where 4.21% of the mean values were greater than or equal to 1.0, indicating a bell shape. Using a ray-tracing model, Pinty *et al.*, (2002) showed surface vegetation that exhibited higher BRF values close to nadir and lower BRF values at larger view zenith angles, typically consisted of sparse foliage clumps on a bright background. Conversely, the mean *k* coefficient for the NIR band does not show any values greater than 1.0 due to the lack of spectral contrast between the canopy and the soil background. The standard deviation of *k* for the red band shows a similar spatial distribution than that of the Θ coefficient standard deviation in the red band, again probably in response to solar zenith angle variation.

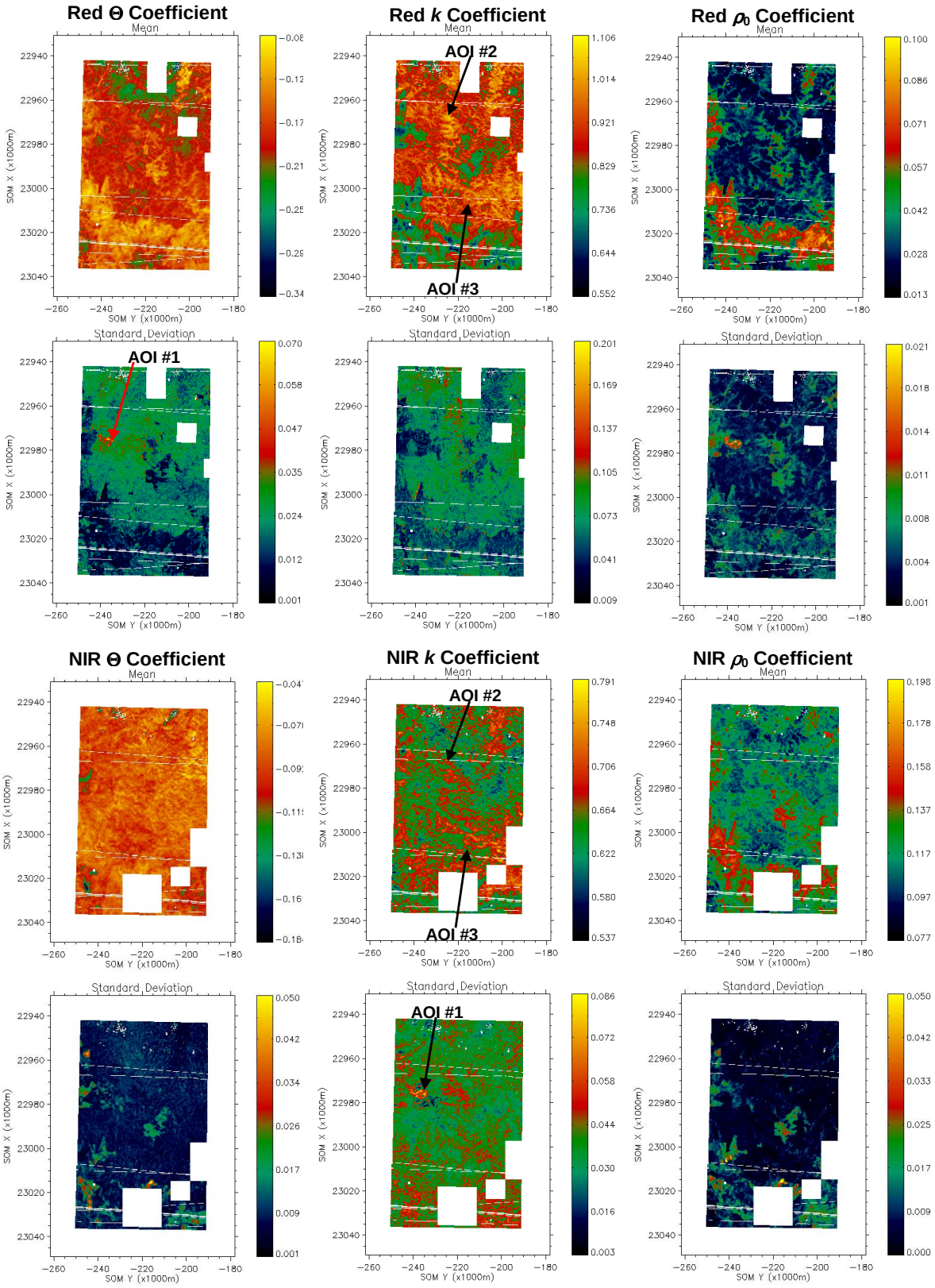


**Figure 8** Rasters of the mean and standard deviation of the RPV model *k* (left), Θ (middle), and $\rho_0$ (right) coefficients derived from the red (top) and NIR (bottom) bands of the MISR Local Mode time series. AOI = Area of interest.

Finally, the spatial-temporal variation in the RPV isotropic coefficient in the red band and the NIR band appear to simply show the overall brightness of the BRF in each band. Spatially consistent patterns in the RPV model coefficients have been commented on qualitatively in numerous publications. Kalluri *et al.* (2001), Gobron and Lajas (2003), and Gobron *et al.* (2002) have all made qualitative interpretations of the spatial organisation of the RPV model coefficients. There were also systematic, interpretable spatial and temporal variations observed over the study site corresponding to known surface variations.

Localised areas of interest (AOI's) are located in Figure 9. The relatively high temporal standard deviation shown in both the RPV and Ross-Li isotropic coefficients at AOI #1 corresponds to an area of woody vegetation regrowth and fieldwork verified a fire went through the area shortly before the 27/09/2003 acquisition. AOI #2 and AOI #3 correspond to woody vegetation of 15.68 and 28.31 FPC, respectively, as defined by the spatially coincident LIDAR plots. It was assumed woody FPC had not changed during the time of observation. Interpretation of the time series in the blue band is inhibited due to the high proportion of missing values and higher error in the atmospheric correction.

For AOI #1 (Figure 9), the RPV model shows an increase in the isotropic coefficient ($\rho_0$) for both the red and green spectral bands, indicating a reduction in photosynthetic activity. In contrast, AOI #2 and #3 do not show this increase and remain relatively constant throughout the time series. The time series for the $\Theta$ coefficient shows the sensitivity of $\Theta$ to solar zenith angle, especially for the 27/09/2003 observation. As solar zenith angles decreases, the effect of shaded background on reflectance anisotropy is minimised, especially in the red band where canopy transmittance in minimised due to chlorophyll absorption (Gerard and North, 1997). It is hypothesised that the reduction in shadow casting results in reduced contrast in $\Theta$ between spectral bands.

The time series for the *k* coefficient is also indicative of the surface change in AOI #1 (Figure 9). The relatively large change in solar zenith angle between 01/08/2003 and 27/09/2003 for AOI #2 and AOI #3 related to the amount of sunlit background diminishing and shaded background increasing. Pinty *et al.* (2002) showed that the potential for *k* to rise above 1 increases under these circumstances, especially as there is distinct spectral contrast between the canopy and the background in the red band, and to a lesser extent in the green band, due to the bright sandy soils characterising the study site. AOI #1 does not show this increase in *k* to above 1, it actually decreases between these dates, suggesting a surface change. *k* in the NIR band still increases like AOI #2 and AOI #3, however this is likely to be due to the relative reduction in reflectance anisotropy due to the radiative dominance of the sunlit background. AOI #2 is consistently above 1, indicating a heterogeneous surface (FPC = 15). Heterogeneity is only exposed at a very low solar zenith angle for AOI #3 (FPC = 28) as due to the effect of shadow casting (Pinty *et al.*, 2002).

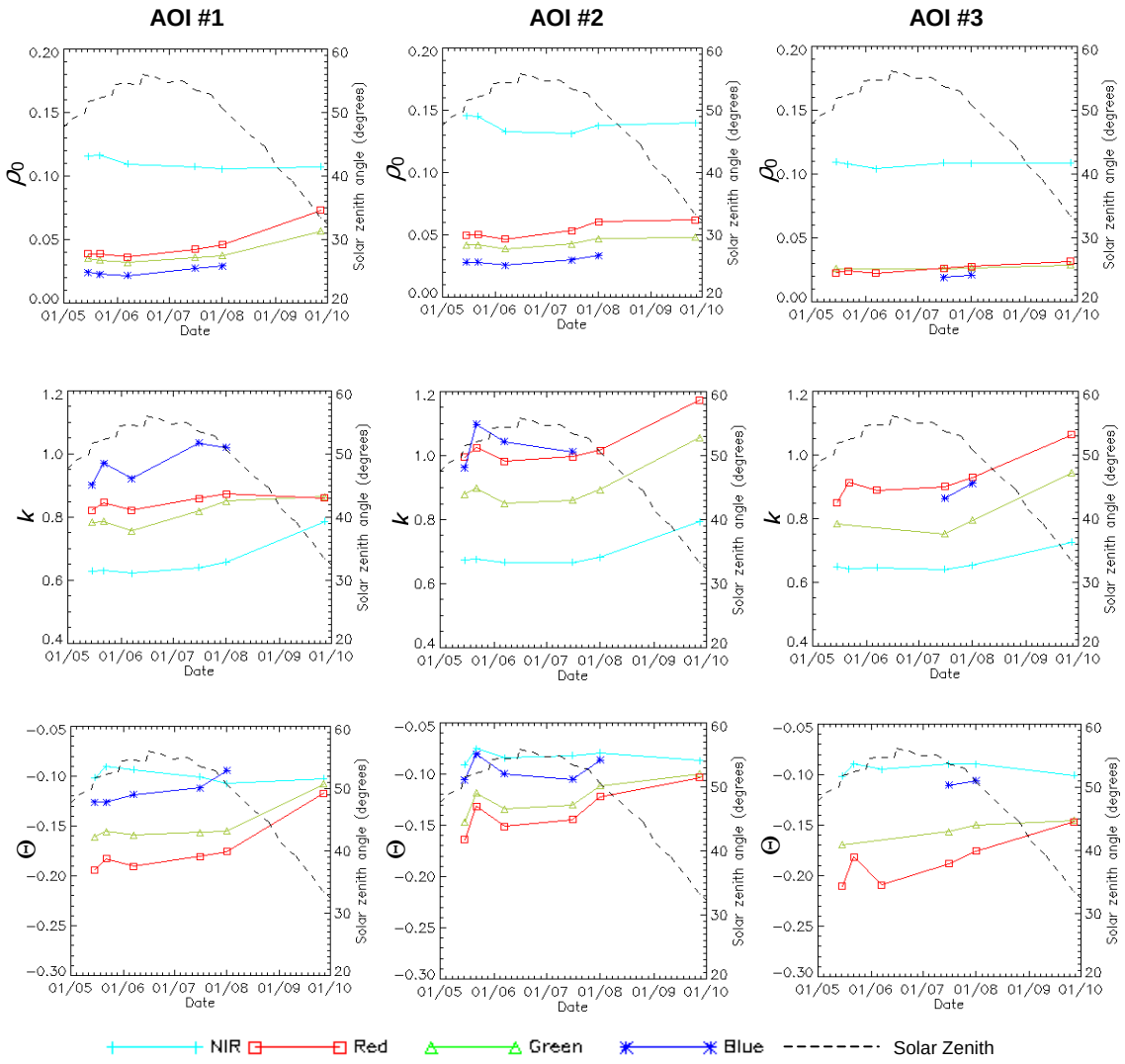


**Figure 9** Time series of a 3 by 3 pixel average of the RPV model coefficients for three AOI's during 2003. AOI #1 (left) is a probable fire scar, AOI #2 (middle) is woody vegetation (FPC = 15.68), and AOI #3 (right) is also woody vegetation (FPC = 28.31).

*LIDAR*

The relationship between LIDAR estimated cover and field estimated foliage projective cover is shown in Figure 10. These plots directly validate the LIDAR estimates of cover and highlight the biases introduced by the sensor. The $R^2$ results in Figure 10 (a) shows a strong correlation between the LIDAR and field measure of FPC ($R^2$ = 0.85, $p$<0.05). Of interest is the outlier beneath the lower prediction interval. This is a result of the field transects underestimating FPC due to subplot heterogeneity. This is not surprising since the LIDAR field transects are not azimuthally independent, however it does show that error does exist in the ground "truth".

The linear regression slope coefficient is less than 1 (0.57), indicating some overestimation bias by the LIDAR. The linear regression offset coefficient is less than 1% FPC, showing, as expected, there is virtually no difference

between LIDAR and field estimates of FPC at zero cover. These observations form the basis of the calibration of LIDAR FPC to field FPC, as the only difference between the significant linear relationships is in the slope coefficient. Figure 10 (b) shows the results of the cross-validation conducted to validate the calibrated LIDAR estimates of FPC ($p$<0.05). The mean RMSE of less than 5% indicates the linear regression offset and slope coefficients were robust and not too sensitive to any particular observations. The departure of the relationship from 1:1 is negligible, despite the lack of observations greater than 50% FPC.

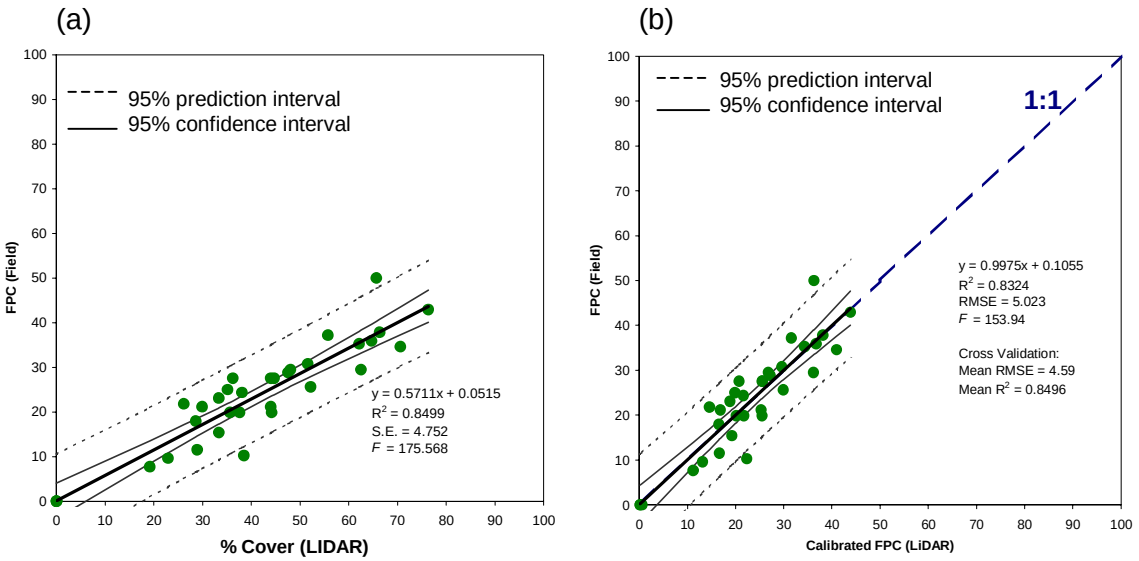


**Figure 10** (a) Field validation of LIDAR FPC for all 33 field plots. (b) Cross validation of field FPC against calibrated LIDAR FPC for all 33 field plots.

These results clearly show that both canopy composition and footprint size of the sensor introduce overestimation bias in FPC. LIDAR data does not distinguish between photosynthetic and non-photosynthetic components of a canopy. Therefore if the photosynthetic foliage is the canopy attribute of interest, especially in open canopies, bias is introduced. Furthermore, the footprint size of the data in this study (≈7cm) may interact with the leaves, which exist with varying orientations and transmittance/reflectance of NIR light. This results in biased FPC estimates, as the partial gaps in foliage within the footprint are not detected. It is important to note that these results are not new findings. These results in Figure 10 are consistent with unpublished independent analyses of the same data by other investigators (Alex Lee, Australian National University, *personal communication*; Trevor Moffiet, University of Newcastle, *personal communication*). Furthermore, the results in this study are of comparable accuracy to independent Australian studies that have validated FPC estimates using field data (Weller *et al.*, 2003; Witte *et al.*, 2000). The effects of footprint size and canopy composition on estimates of FPC are well documented (Lovell *et al.*, 2003; Weller *et al.*, 2003; Witte *et al.*, 2000), and current work is aimed at improving LIDAR estimates of FPC.

*Comparison of FPC and Model Coefficients*

Figure 11 presents significant correlations ($p < 0.05$) between LIDAR estimates of FPC and the RPV coefficients the 01/08/2003 and 27/09/2003 MISR acquisitions. Note that only comparisons with FPC for the red band are shown, as all other comparisons were uncorrelated. Additionally, polynomials were only fitted to the 27/09/2003 acquisitions as these provided the best inversion accuracy. The isotropic coefficient for the RPV model shows the highest correlation ($R^2 = 0.44$) to FPC. This is not surprising as increased amounts of foliage absorb more irradiance, and has been documented by other authors to be related to the amplitude rather than the shape of the BRDF (Gao *et al.* 2003; Lovell and Graetz, 2002). Note that the magnitude of the isotropic coefficient does not change between dates.

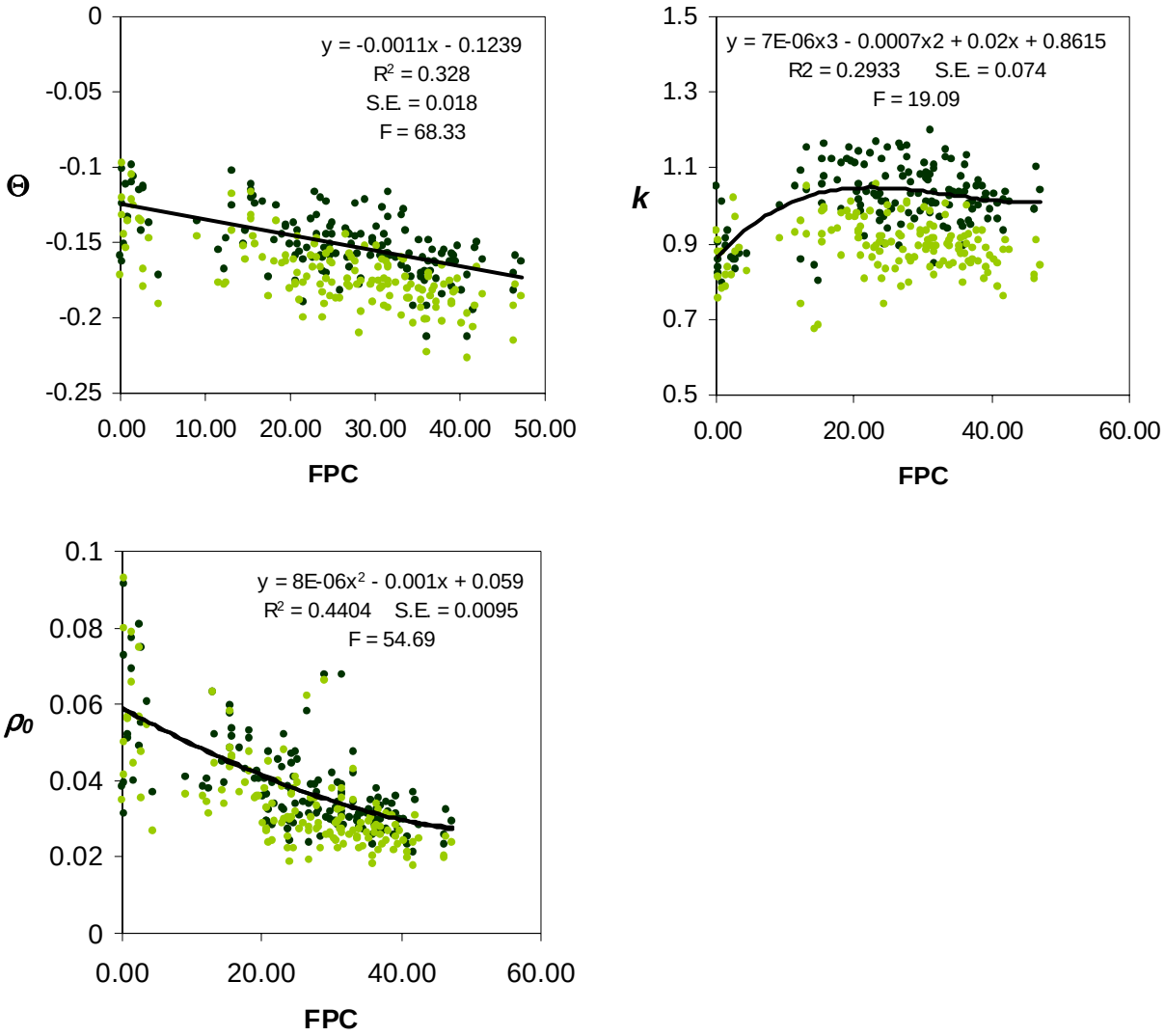


**Figure 11** Regression of FPC and the RPV model coefficients. The green dots represent 01/08/2003 MISR observations (SZA ≈ 51°) and the black dots represent 27/09/2003 MISR observations (SZA ≈ 33°). SZA = solar zenith angle.

Although weaker, the *k* and Θ RPV coefficients also display systematic interpretable trends ($R^2$ = 0.29 and 0.33, respectively). Low FPC observations exhibit "bowl" shaped anisotropy, thus are radiatively homogenous at the MISR spatial resolution, and medium FPC observations exhibit "bell" shaped anisotropy, and thus are radiatively heterogeneous at MISR spatial resolution. This trend is not as noticeable for the 01/08/2003 MISR acquisition, most probably due to the effects of shadowing at the higher solar zenith angle. It is expected that if high FPC (>50%) observations were included, they would exhibit "bowl" shaped anisotropy again due to the obscuration of sunlit background at low view zenith angles. The degree of backscattering (Θ) increases with FPC and is related to the relative reduction of sunlit background and increase in sunlit crown and shaded background (Gerard and North, 1997).

The comparisons shown only weakly correspond to findings of previous studies exploring the relationship between the BRDF and vegetation structure (Pinty *et al.*, 2002; Lovell and Graetz, 2002). Data and analysis problems have limited the comparisons and may well have concealed underlying relationships. These problems include the variable sampling density of the LIDAR instrument due to windy conditions at the time of acquisition. In particular, the limited spatial extent of the LIDAR plots in comparison to the spatial resolution of the MISR data may mean the ground data were not representative. This suggests further research to link field plot measurements of vegetation structure to the spatial resolution of MISR is required. Emphasis is still placed on the scaling strategy of Woodcock *et al.* (1997), where intermediate scale estimates of vegetation structure would be aggregated to the scale of MISR and then used to calibrate and validate relationships between vegetation structure and surface reflectance anisotropy. Alternatives to LIDAR would obviously include SAR (Lucas *et al.*, 2001) and, for FPC only, Landsat data (Danaher *et al.*, 2004).

## Conclusions

1. Discrete scanning airborne LIDAR is an effective tool for FPC, provided that the biases introduced by sensor sampling limitations are understood.

There were highly significant relationships between the field and LIDAR derived estimates of FPC, however interactions between the LIDAR footprint size, sampling density and FPC in the SBB mean the LIDAR estimates contain bias. The calibration of LIDAR estimated cover, using field estimates of FPC, is currently an avenue of research that is being further developed by SLATS (Danaher *et al.*, 2004). LIDAR shows significant promise as a sampling tool for characterising vegetation structure at the sub-pixel scale of coarse resolution MVA sensors such as MISR. This is reflected by other studies integrating optical and SAR data with LIDAR (e.g. Lucas *et al.*, 2001).

2. Semi-empirical BRDF model coefficients can be used to characterise surface reflectance anisotropy in the Queensland SBB. However their sensitivity to vegetation structure requires further research.

This study successfully characterised the spectral directional reflectance of the land surface in the Queensland SBB Biogeographic Region. The moving-window OLS regression technique developed in this study resulted in a spatially consistent representation of the surface BRF. This development allows Local Mode MISR data to be used for the characterization of surface reflectance anisotropy, without the need to apply complex atmospheric radiative transfer algorithms. It is evident from the results that the RPV model coefficients display coherent spatial and temporal variations corresponding to known variations in vegetation structure within the SBB. This is the first time semi-empirical BRDF models have been compared and related to the land surface using MISR data in Australia. The RPV model was more accurate than the Ross-Li model in characterising surface reflectance anisotropy. Therefore, it is appropriate for future work attempting to link MISR data to the land surface in Queensland.

3. There are interpretable relationships between LIDAR estimated FPC and the RPV model coefficients, however a quantitative evaluation of their significance is the subject of further study.

This study showed a simple empirical comparison between the spectral directional reflectance of the land surface and FPC in the Queensland SBB, therefore it builds on the few studies conducted on the empirical relationship between the BRDF and vegetation structure in Australia (Lovell and Graetz, 2002; Grant, 2000). Future work will aim to assess MISR data for improving the discrimination of woody and herbaceous vegetation types and the detection of woody vegetation change in Queensland. This study was unique in that it linked remotely sensed datasets that have been used to characterise vegetation structure but have differing spatial resolutions and extents, acquisition characteristics, and errors. Whilst the same empirical relationships may not be observed outside the locality of the study site, especially where there is less spectral contrast between the canopy and its background, the results from this study are unique in the context of vegetation remote sensing in Queensland.

## Acknowledgments

The University of Queensland (UQ), Bureau of Rural Sciences, Department of Natural Resources and Mines, CRC for Carbon Accounting, and affiliated organisations are acknowledged for the provision of data and/or financial support. NR&M Climate Impacts and Natural Resource Systems and UQ Biophysical Remote Sensing Group members are acknowledged for useful discussions and technical assistance. The JPL-MISR team are acknowledged for the provision of Local Mode MISR data.

## References

Abdou, W., Pilorz, S., Helmlinger, M., Diner, D., Conel, J. & Martonchik, J. 2002. *Sua Pan Surface Bidirectional Reflectance: A Validation Experiment of*

*the Multi-angle Imaging SpectroRadiometer (MISR) During SAFARI 2000*. Jet Propulsion Laboratory, California Institute of Technology.

Asner, G., Braswell, B., Schimel, D. & Wessman, C. 1998. Ecological research needs from multiangle remote sensing data. *Remote Sensing of Environment*, 63: 155-165.

AUSLIG, 1990, *Atlas of Australian Resources*, Third Series, Volume 6, Vegetation (Canberra: Australian Surveying and Land Information Group, Department of Administrative Services).

Burrows, W., Henry, B., Back, P., Hoffman, M., Tait, L., Anderson, E., Menke, N., Danaher, T., Carter, J., & McKeon, G. 2002. Growth and carbon stock change in eucalypt woodlands in northeast Australia: Ecological and greenhouse sink implications. *Global Change Biology*, 8: 769-784.

Danaher, T.J. 2002. An empirical BRDF correction for Landsat TM and ETM+ imagery. *Proceedings of the 11th Australasian Remote Sensing and Photogrammetry Conference*, Brisbane, Australia, September 2002.

Danaher, T.J., Armston, J.D. & Collett, L.J. 2004. A multiple regression model for the estimation of woody foliage cover using Landsat in Queensland, Australia. *Proceedings of IGARSS 2004, Anchorage*.

Danaher, T.J., Wedderburn-Bisshop, G.R., Kastanis, L.E. & Carter, J.O. 1998. The Statewide Landcover and Trees Study (SLATS) – Monitoring land cover change and greenhouse gas emissions in Queensland. *Proceedings of the 9th Australasian Remote Sensing and Photogrammetry Conference*.

Diner, D., Beckert, J., Reilly, T., Bruegge, C., Conel, J., Kahn, R., Martonchik, J., Ackerman, T., Davies, R., Gerstl, S.A., Gordon, H., Muller, J., Myneni, R., Sellers, P., Pinty, B. & Verstraete, M. 1998. Multi-angle Imaging SpectroRadiometer (MISR): Instrument description and experiment overview. *IEEE Transactions on Geoscience and Remote Sensing*, 36(4): 1072-1087.

Diner, D., Martonchik, J., Borel, C., Gerstl, S., Gordon, H., Knyazikhin, Y., Myneni, R. Pinty, B. & Verstraete, M. 1999. *MISR: Level 2 Surface Retrieval Algorithm Theoretical Basis (Revision D)*. Jet Propulsion Laboratory, California Institute of Technology.

Gao, F., Schaaf, C., Strahler, A., Jin, Y., & Li, X. 2003. Detecting vegetation structure using a kernel-based BRDF model. *Remote Sensing of Environment*, 86: 198-205.

Gerard, F. & North, P. 1997. Analyzing the effect of structural variability and canopy gaps on forest BRDF using a geometric-optical model. *Remote Sensing of Environment*, 62: 46-62.

Gobron, N. & Lajas, D. 2002. A new inversion scheme for the RPV model. *Canadian Journal of Remote Sensing*, 28(2): 156-167.

Gobron, N., Pinty, B., Verstraete, M.M., Widlowski, J., & Diner, D.J. 2002. Uniqueness of multi-angular measurements – Part II: Joint retrieval of vegetation structure and photosynthetic activity from MISR. *IEEE Transactions on Geoscience and Remote Sensing*, 40(7): 1574-1592.

Grant, I.F. 2000. Investigation into the variability of the directional reflectance of Australian land cover types. *Remote Sensing Reviews*, 19: 243-258.

Henry, B., Danaher, T., McKeon, G. & Burrows, W. 2002. A review of the potential role of greenhouse gas abatement in native vegetation management in Queensland's rangelands. *The Rangeland Journal*, 24(1): 112-132.

Hu, B., Lucht, W., Li, X. & Strahler, A.H. 1997. Validation of kernel-driven semiempirical models for the surface bidirectional reflectance distribution function of land surfaces. *Remote Sensing of Environment*, 62: 201-214.

Jupp, D.L.B. & Walker, J. 1996. Detecting structural and growth changes in woodlands and forests: The challenge for remote sensing and the role of geometric-optical modelling. In: Gholz, H.L., Nakane, K. and Shimoda, H. (eds). *The Use of Remote Sensing in the Modelling of Forest Productivity*. Kluwer Academic Publishers, Dordrecht, The Netherlands, pp. 75-108.

Kalluri, S., Zhang, Z., Jaja, J., Liang, S. & Townshend, J. 2001. Characterizing land surface anisotropy from AVHRR data at a global scale using high performance computing. *International Journal of Remote Sensing*, 22(11): 2171-2191.

Li, X. & Strahler, A.H. 1992. Geometric-optical bi-directional reflectance modelling of the discrete crown vegetation canopy: Effect of crown shape and mutual shadowing. *IEEE Transactions on Geoscience and Remote Sensing*, 30(2): 276-292.

Lovell, J.L. & Graetz, R.D. 2002. Analysis of POLDER-ADEOS data for the Australian continent: The relationship between BRDF and vegetation structure. *International Journal of Remote Sensing*, 23(14): 2767-2796.

Lovell, J.L., Jupp, D.L.B., Culvenor, D.S. & Coops, N.C. 2003. Using airborne and ground-based ranging Lidar to measure canopy structure in Australian forests. *Canadian Journal of Remote Sensing*, 29(5): 607-622.

Lucas, R.M., Tickle, P., Witte, C. & Milne, A.K. 2001. Development of multistage procedures for quantifying the biomass, structure and community composition of Australian woodlands using polarimetric radar and optical data. *Proceedings of IGARSS 2001*, Sydney.

Lucht, W., Barker Schaaf, C. & Strahler, A.H. 2000. An algorithm for the retrieval of albedo from space using semiempirical BRDF models. *IEEE Transactions on Geoscience and Remote Sensing*, 38(2): 977-998.

Maignan, F., Br on, F.M. & Lacaze, R. 2004. Bidirectional reflectance of Earth targets: Evaluation of analytical models using a large set of spaceborne measurements with emphasis on the hot spot. *Remote Sensing of Environment*, 90: 210-220.

Markwardt, C. 2002 (updated 30 May 2004), *'IDL curve fitting and optimization'*, University of Wisconsin-Madison. Retrieved 10 May 2004 from http://astrog.physics.wisc.edu/~craigm/idl/fitting.html

Martonchik, J.V., Bruegge, C.J. & Strahler, A.H. 2000. A review of reflectance nomenclature used in remote sensing. *Remote Sensing Reviews*, 19: 9-20.

Pinty, B., Widlowski, J., Gobron, N., Verstraete, M.M., & Diner, D.J. 2002 Uniqueness of multi-angular measurements – Part I: An indicator of subpixel surface heterogeneity from MISR. *IEEE Transactions on Geoscience and Remote Sensing*, 40(7): 1560-1573.

Rahman, H., Pinty, B, & Verstraete, M. 1993. Coupled surface-atmosphere reflectance (CSAR) model: 2. Semiempirical surface model usable with NOAA advanced very high resolution radiometer data. *Journal of Geophysical Research*, 98: 20791-20801.

Roujean, J-L., Leroy, M. & Deschamps, P-Y. 1992. A bidirectional reflectance model of the Earth's surface for the correction of remote sensing data. *Journal of Geophysical Research*, 97(D18): 20,455-20,468.

RSI (2004). IDL –Interactive Data Language. Boulder, CO 80301, USA, Research Systems Inc.

Specht, R.L. 1970. Vegetation. In: *The Australian Environment*. 4th ed. Leeper, G.W. (ed). CSIRO, Melbourne University Press, Melbourne, Australia.

Specht, R.L. & Specht, A. 1999. *Australian Plant Communities: Dynamics of Structure, Growth and Biodiversity.* Oxford University Press.

Tickle, P.K., Witte, C., Lee, A., Lucas, R.M., Jones, K. & Austin, J. 2001. Use of airborne scanning LIDAR and large scale aerial photography within a strategic forest inventory framework. *Proceedings of IGARSS 2001*, Sydney.

Wanner, W., Li, X. & Strahler, A.H. 1995. On the derivation of kernels for kernel-driven models of bi-directional reflectance. *Journal of Geophysical Research*, 100(D10): 21,077-21,089.

Weller, D., Denham, R., Witte, C., Mackie, C. & Smith, D. 2003. Assessment and monitoring of foliage projected cover and canopy height across native vegetation in Queensland, Australia, using laser profiler data. *Canadian Journal of Remote Sensing*, 26(5): 578-591.

Witte, C., Denham, R., Turton, D., Jonas, D., Tickle, P. & Norman, P.2000. Airborne Laser Scanning – A tool for monitoring and assessing the forests and woodlands of Australia. *Proceedings of the 10th Australasian Remote Sensing and Photogrammetry Conference*, Adelaide, Australia, September 2000.

Woodcock, C., Collins, J. & Jupp, D. 1997. Scaling remote sensing models. In: van Gardingen, P., Foody, G. and Curran, P. (eds). *Scaling-Up From Cell to Landscape*. Cambridge University Press, United Kingdom, pp. 61-77.

Zhang, K., Chen, S., Whitman, D., Shyu, M., Yan, J. & Zhang, C. 2003. A progressive morphological filter for removing nonground measurements from airborne LIDAR data. *IEEE Transactions on Geoscience and Remote Sensing*, 41(4): 872-882.